Electronic Supplementary Material (ESI) for Nanoscale

Electronic Supplementary Information for manuscript

"*Fundamental quantum noise mapping with tunnelling microscopes tested with subatomic spatial resolution*"

Markus Herz, Samuel Bouvron, Elizabeta Ćavar, Mikhail Fonin, Wolfgang Belzig, and Elke Scheer

Department of Physics, University of Konstanz, D-78457 Konstanz, Germany

1. **Schematic diagram of the noise measurement setup**
2. **Sample preparation**
3. **Quantitative analysis of the topography**
4. **Examples of spectra and breakdown of major detector noise components**
5. **Calibration of the analogue noise signal**
6. **Residual scanner drift correction**
7. **Statistics of the Fano factors for spatial noise mapping**
8. **References**

1. Schematic diagram of the noise measurement setup

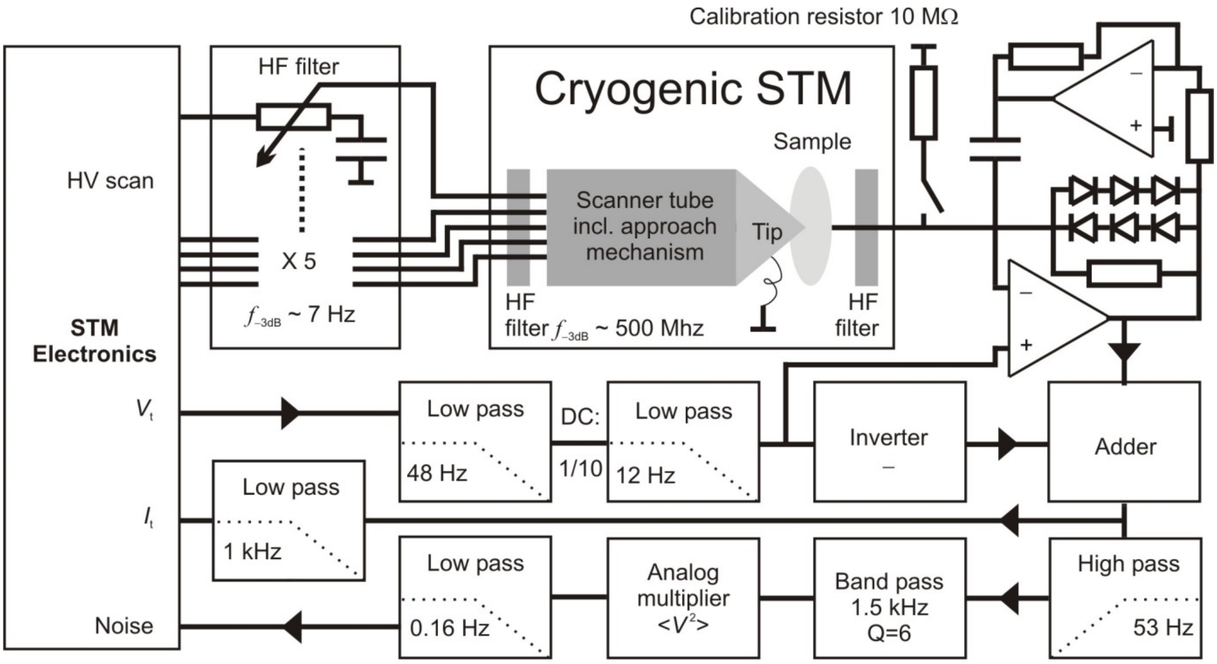

Fig. S1. Schematic diagram of the STM measurement electronics.

Figure S1 shows a schematic diagram of the STM measurement electronics. Active filtering is applied to the tunnelling voltage, allowing for a $10^{-18}V^2$/Hz noise level at the "+" input of the IVC, and with respect to ground potential. The total noise is in the order of $2{\cdot}10^{-17}V^2$/Hz at the "–" input of the IVC, and above 1 kHz. It is also possible to apply the voltage to the tip and to ground the "+" input of the IVC. The tunable capacitive compensation extends the bandwidth of the IVC by approximately half an order of magnitude into the kHz range useful for fast scanning, see Ref. [S1]. The band-limited current signal of the IVC is split into DC and AC components, the latter being squared in a pre-selected frequency band and low-pass filtered for readout. A calibration resistor with a negligible capacitance compared to the total input capacitance of ~0.3 nF is connected to the input of the IVC at retracted tip. It produces an effective input current noise according to its Johnson current noise to be absorbed and displayed by the IVC within its measurement band. This signal can be used for calibrating the noise measurement, see section 3. In contrast to standard STM electronics, the piezo actuation high voltages are low-pass filtered with a –3dB bandwidth of <10 Hz. This is a way to avoid significant cross-talk of tunnelling barrier geometric vibrations to current noise that are caused by electronic noise on the high voltage lines. The tunnelling current (TC) is extremely sensitive w.r.t. barrier geometric vibrations and changes by roughly one order of magnitude for a 0.1 nm displacement. Our data and modelling show that a geometric stability of the barrier in the order of <1 fm/$\sqrt{Hz}$ could be reached by filtering, which supports extremely low noise measurements of the TC. The geometric noise contribution is multiplied with the local TC gradients and squared. It cannot be easily calibrated. This is the reason why it is damped by low pass filtering, to avoid any additional calibrations that might become necessary otherwise. The piezo filters have been realized using passive low pass filters on the high voltage lines, see Fig. S1.

2. Sample preparation

The Ir (111) single crystal was cleaned by repeated cycles of Ar^+ sputtering while keeping the sample at room temperature ($p_{Ar} = 5\times10^{-4}$Pa, 2 keV), flash annealing at about 1400 K, followed by annealing in oxygen atmosphere ($p_{O2} = 1\times10^{-5}$Pa) at about 950 K, and subsequent flash annealing in ultra high vacuum to about 1400 K. The quality of the Ir(111) surface was checked by low energy electron diffraction (LEED) and STM.

3. Quantitative analysis of the topography

Figure S2a shows cross-sections of constant TC traces at different TC values performed above the highly corrugated molecular orbital structure shown in Figure 1c of the main text. Additionally, Figure S2b shows a cross-section in *z*-direction of the TC above the peaks, at fixed (*x*,*y*) position, where *x* and *y* denote the in-plane coordinates and *z* the out-of-plane coordinate. In addition we plot in Figure S2b the locations of the centres of circles fitted to the curvature in the direction of the cross-section (*x*-*z*-plane). These circle centre positions are obtained from a fit, as indicated by the dashed circles in Figure S2a.

This analysis reveals a mainly exponential TC decay above the topographic maxima of the scan traces. The exponential decay is caused by the overlap of atomic basis functions with near exponential radial component at sufficiently large distance from the nuclei.[S2,S3] When fitting with an $e^{-2\kappa r}$ dependency in the vertical direction, we deduce an approximate experimental value of κ = 7.8/nm for the decay constant, that is markedly smaller than the theoretical value of 11.7/nm determined assuming the literature value for the work function of Ir (5.27 eV, Ref. S4). However, the discrepancy is in line with observations made for more than three decades.[S5,S6] Although the influence of the non-exponential decay is not negligible and has been suggested earlier to be at the origin of this deviation[S6], this proposition has never been studied quantitatively before.

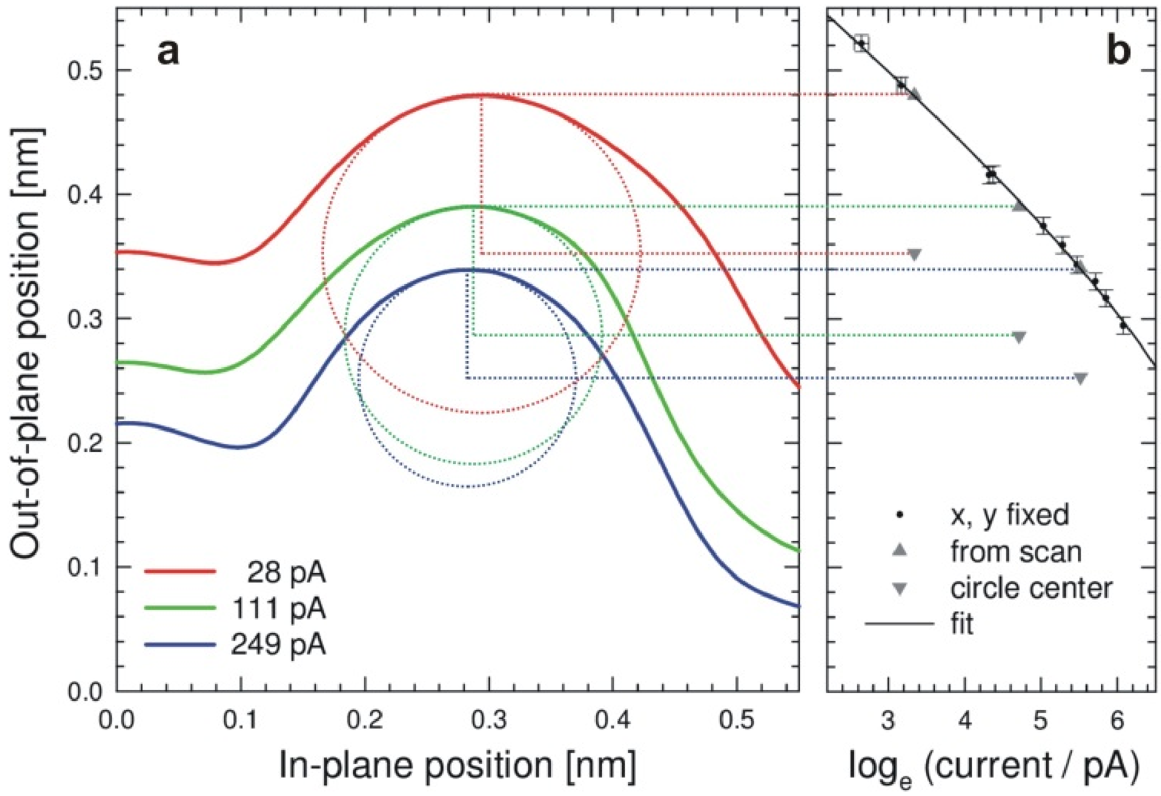

Fig. S2. a: Cross-sections of constant tunnelling current (TC) traces at different TC values performed above the structure shown in Figure 1c of the main document, and a voltage of 11.5 mV. **b**: Vertical cross-section of TC measured above the image maxima, and the vertical locations of centres of circles fitted to the curvature at the topographic maximum, in the direction of the cross-section. The motion of the fitted circle centres when changing the TC is caused by the non-spherical distribution of the TC with respect to the nuclei. The quantities *x* and *y* correspond to the positions in the fast and slow in-plane scan directions, respectively.

To address this open question the out-of-plane distribution of the TC is explored in more detail. It can be seen from Figure S2a that the topographic maximum of the constant TC image moves to slightly smaller in-plane position (*x*-direction) when the set-point of the TC is increased. Such a coordinate shift may explain part of the lowering of the measured topographic height (out-of-plane position) at the higher TC values shown in Figure S2b, compared to what an extrapolation of a linear fit of the data performed for the lower TC values would suggest. However, as the comparison shows, the effect is negligible and cannot explain the experimental curve observed here.

Remarkably, full tunnelling theory can directly explain the deviations from exponential dependence given by non-exponential radial components of the atomic basis functions of the conduction electrons of Ir, i.e. $n = 5$ shells. Here, n is the energy quantum number. Even for tunnelling between *s*-electrons a small deviation from a pure exponential behaviour is expected owing to the electron density radial factor $r^{2(n-1)}e^{-2\kappa r}$ in the far limit.[S2,S3] However, the deviations of the TC from exponential behaviour are expected to be smaller, when higher angular momentum tip- and sample states interact with each other. The strong angular confinement of the tunnelling matrix elements of the higher angular momentum states of both tip and sample results in a focusing effect that in turn gives rise to a reduction of the *deviations* from the exponential behaviour of the TC. We tentatively fit the residual deviations from the exponential decay according to $e^{-2\kappa z}L_2^5(2\kappa(z-z_0))^2$ that includes a focusing factor $(z-z_0)^{-4}$ for $l = 2$, hydrogen-type states of Ir. Here $L_{n-l-1}^{2l+1}(2\kappa r)$ are the generalized Laguerre polynomials that appear in the radial functions of hydrogen-like orbitals of quantum number $n = 5$, angular momentum $l = 2$ and distance r from the nucleus. The focusing factor results from using a fixed angle factor for interactions of confined orbital lobes. With the nominal value of $\kappa = 11.7$/nm we find $z_0 = -0.5$ nm as only fit parameter, and referring to the coordinate frame of Figure S2. The fitting is shown as line in Figure S2b. It excellently describes the experimentally observed data. We note that although our model is simplified, it confirms that the cross-sections were indeed recorded at relatively large tunnel distance. Without assuming a focusing factor, even larger distances between tip and sample would result, that are rather unlikely. The radius of the fitted circles is extremely low due to $l = 2$ states presumably at both tip and sample. Using smaller values for the angular momentum would result in much larger curvature radii and cannot explain the experimental observations. The observed motion of the circle centres as a function of the TC is the consequence of the overlap of higher angular momentum states with sharp lobes of the wave functions that produce the highly corrugated, non-spherical TC distribution with respect to the nuclei[S2,S3].

Summarizing, we demonstrated that in STM the geometric effects of orbital interactions play an important role. The corrugation can exhibit very small features with very high curvature, especially when they are present at both tip and sample. The scan traces have been acquired at distances where the short-range forces between tip and sample are typically in the order of or below 10^{-2} nN, and elastic deformations account to picometres at most[S7,S8].

4. Examples of spectra and breakdown of major detector noise components

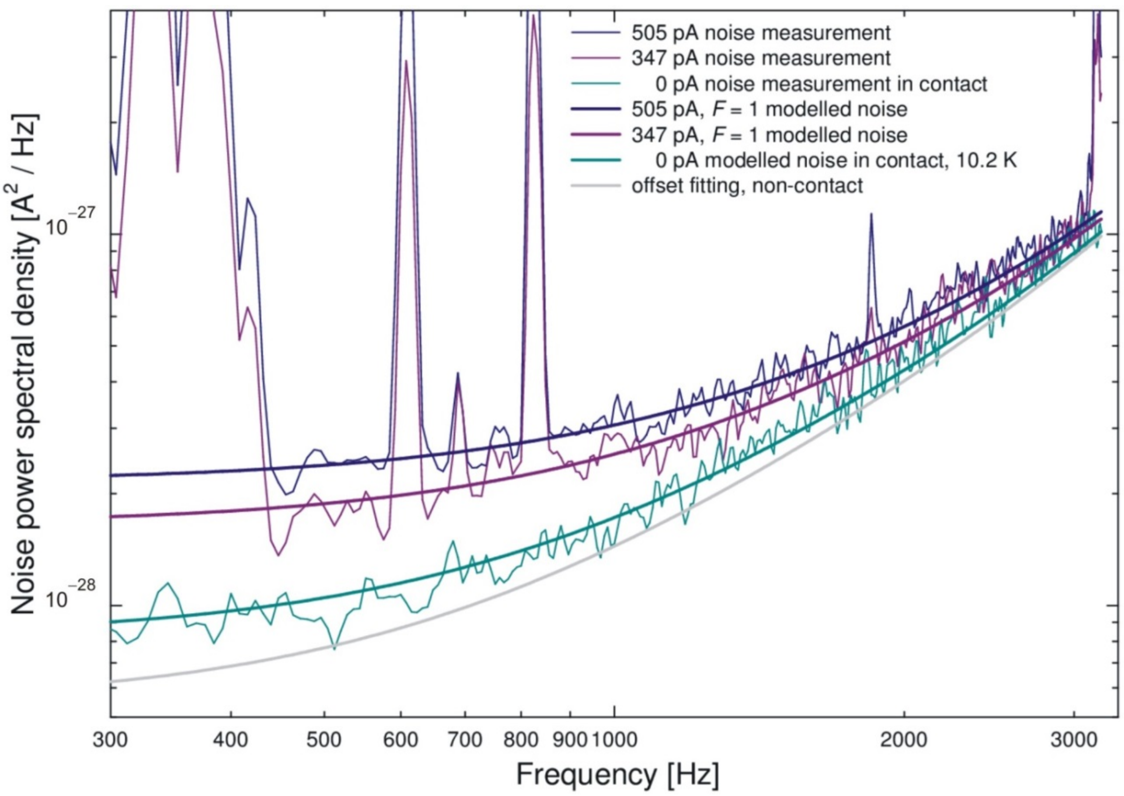

Fig. S3. Examples of tunnelling current (TC) spectra acquired with the STM in contact and noise modelling, using the electronic setup depicted in Fig. S1, and the STM at temperatures of a few Kelvin. The offset fitting has been performed for a number of spectra acquired with retracted tip. Tunnelling resistance for the noise measurements: $2x10^7$ Ω. Piezo low-pass filtering with −3 dB bandwidths of ~7 Hz and ~500 MHz is engaged. Despite of successfully damping f^{-2} contributions with the ~7 Hz filters, and that are caused by piezo actuator electronic noise, additional disturbance lines emerge when switching on the TC in contact. These are caused by vibrations in the tunnel contact. The noise is measured far enough from the lines with the analogue, calibrated power measurement system shown in Fig. S1 to obtain the total noise power. Before fitting, the spectra have been corrected for bandwidth effects of the amplifier, to obtain equal spectral weight for all frequencies. This numeric fitting is not necessary for the analogue noise measurement and calibration described in the respective sections.

Figure S3 shows examples of TC noise spectra acquired with the STM in contact and noise modelling, using the measurement setup shown in Fig. S1. Between 900 Hz and 1.9 kHz the spectra are free from disturbance lines. This frequency window is used for the determination of the shot noise signal. From the linear increase of the noise level in this window it can be clearly seen that TC noise components with F = 1 add to the amplifier offset. The latter has been determined by fitting a number of spectra acquired with retracted tip, and without assuming any noise model.

The total measured power spectral density is approximately given by

$$n_{I^2} = S + 4k_B T / R_{FB} + \left(2\pi\, f\, C_{in}\, n_V(f)\right)^2 \qquad (1),$$

where R_{FB} is the value of the feedback resistor that is at room temperature, C_{in} is the total input capacitance of the current sensing wire w.r.t. ground potential, n_V is the voltage noise spectral density of the amplifier. The third term of the right side of (1) can be understood in the way that inside its bandwidth, the IVC will compensate for its input voltage noise by charging the input capacitance. This term is the largest detector noise component at higher frequencies.

The offset noise fitting in Fig. S3 can be explained by a background constant noise component of $5.7 \cdot 10^{-29}$ A^2/Hz that is mainly caused by the feedback resistor of the amplifier, and a total voltage noise of $n_V = 2.2 \cdot 10^{-17}$ V^2/Hz, assuming a total input capacitance of 335 pF, including the amplifier contribution. The value of n_V is depending on frequency, showing 1/f-contributions at lower frequencies. These are neglected in the modelling described here, since they are also subtracted via the calibration procedure described in the next section.

We note that although $1/f^2$ noise from piezo electronic cross-talk seems to be suppressed completely by using the piezo low-pass filters, frequently this $1/f^2$ noise is still visible below 1 kHz. This occurs at highly corrugated structures such as atoms on the surface. In this case, the 4-fold higher sensitivities of the x- and y- anti-symmetric single electrode voltages of the piezo scanner tube produce a roughly threefold higher linear mechanical noise, compared to the *z*-axis. This noise contribution is again multiplied with the local TC gradients and squared, and cannot be easily calibrated. This is the reason why the piezo filters are used, avoiding this noise component. Tests of different bandwidths of the different electrode types have been performed. Different DAC outputs for the high voltages amplifier inputs can also produce slightly different noise levels.

When the spectra have been controlled to display white noise, the *S* measurements begin. To avoid uncertainties that could be introduced by fitting or processing of spectra, the analogue squared signal of the AC-components around a fixed central frequency is measured, see Fig. S1. It is directly proportional to the total noise power spectral density in absence of disturbance lines. The remaining task to obtain the measured noise spectral density is then to subtract the amplifier noise offset and calibrate the analogue noise signal.

5. Calibration of the analogue noise signal

The calibration is performed by connecting the reference resistor R_c of Fig. S1 to the input of the IVC and measuring the output change in the spectrum and the squared analogue noise power signal.

According to equation (3) of the main document, the measured noise power spectral density is given by

$$S = \frac{4k_B T_{R_c}}{R_c} \frac{V_{Noise,contact} - V_{Noise,0}}{V_{Noise,R_c} - V_{Noise,0}} = \frac{4k_B T_{R_c}}{R_c} \frac{g^2 \int_0^\infty S\, w(f)\, df}{g^2 \int_0^\infty \frac{4k_B T_{R_c}}{R_c} w(f)\, df} \qquad (2),$$

where R_c is the calibration resistor and T_{R_c} its temperature.

The squared noise signal V_{Noise} is the direct analogue of the total integrated noise power spectral density in the filter band. For calibration with a fixed filter transfer function, the offset noise $V_{Noise,0}$ is removed from both calibration and contact noise measurement V_{Noise,R_c} and $V_{Noise,contact}$, respectively. This is valid because the noises are not correlated and the average of their products vanishes in the squared signal. The calibration resistor has a negligible capacitance compared to the total input capacitance of ~0.3 nF and can be switched to the input of the IVC at retracted tip. The calibration does not include additional changes of the total noise signal due to very small changes of the tip-sample capacitance according to formula (1) of this document. Possible effects are discussed in the main document. Further, it was tested that the measured noise does not depend on the current through this reference resistor. This shows that the measured noise is simply the sum of the noise powers of the measurement electronics and the tip-sample contact in the STM. Quantitatively, a value of $R_c = 10\ \mathrm{M\Omega}$ that simulates a TC noise of 5.1 nA has shown to be useful.

6. Residual scanner drift correction

The topographic height of every data point has been corrected by taking data points and images at equally spaced times, starting from a low TC value to higher TC values and going to the low TC value again. The vertical drift in the overall time interval is divided by the number of TC steps, to calculate a height correction for every vertical step. We check the validity of the procedure by comparing “approach” and “retract” heights and conform that they fall on the same height.

7. Statistics of the Fano factors for spatial noise mapping

Figure S4 shows the statistics of the Fano factors for the spatial noise mapping shown in Figure 3 of the main document, evaluated per pixel of the shown scan range.

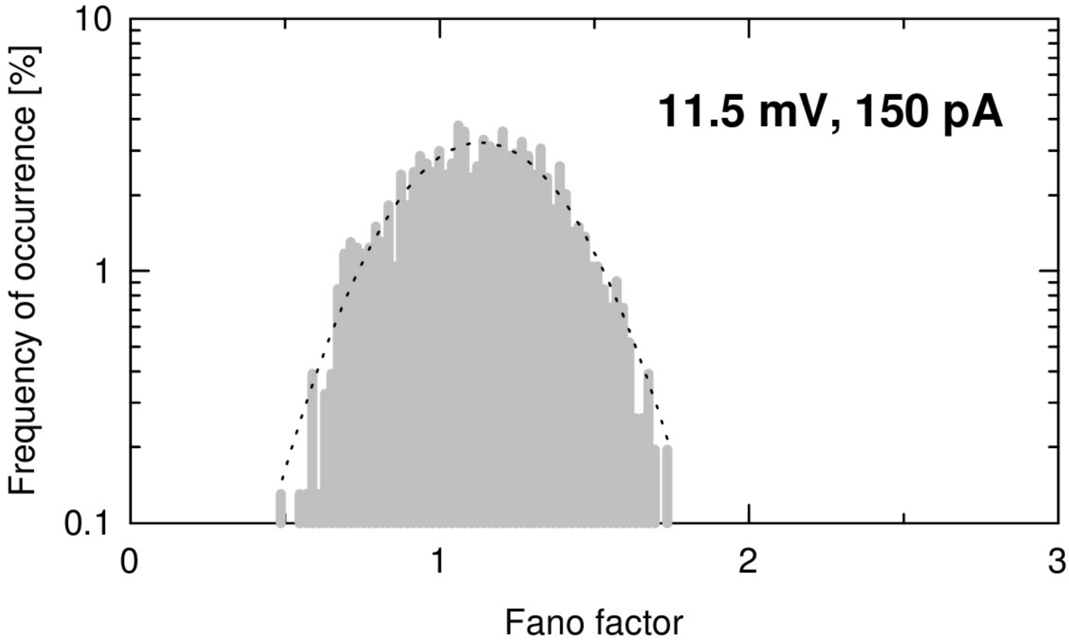

Fig. S4. Statistics of the Fano factors for the spatial noise mapping shown in Figure 3 of the main document. The dashed line represents a fitting with a normal distribution.

In the logarithmic diagram, the nearly parabolic shape of the distribution of the Fano factor readouts is caused by the statistical properties of the measurement mainly determined by detector noise. A fitting, indicated in Fig S4 as dashed line, with a normal distribution results in $F = 1.13 \pm 0.26$. The standard deviation of these image data containing six scan-lines is slightly bigger than the corresponding rms-deviation of five scan-lines in the main document, $F = 1.13 \pm 0.18$. The Fano factor scan line shown in Figure 3 of the main document shows a narrower distribution, because it has been obtained by averaging over five neighbouring pixels in *y* direction..

8. References

S1 U. Dürig, L. Novotny, B. Michel and A. Stalder, *Rev. Sci. Instrum.* 1997, **68**, 3814.

S2 M. Herz, F. J. Giessibl and J. Mannhart, *Phys. Rev. B* 2003, **68**, 045301.

S3 C. J. Chen, *Introduction to Scanning Tunneling Microscopy;* Oxford University Press: Oxford, New York, USA, 1993.

S4 W.M. Haynes, *CRC Handbook of Chemistry and Physics*, CRC Press: Boca Raton, London, United Kingdom, 2012.

S5 G. Binnig, H. Rohrer, Ch. Gerber and E. Weibel, *Appl. Phys. Lett.* 1982, **40**, 178.

S6 M. Herz, Ch. Schiller, F. J. Giessibl and J. Mannhart, *Appl. Phys. Lett.* 2005, **86**, 153101.

S7 J. Welker and F. J. Giessibl, Revealing the angular symmetry of chemical bonds by atomic force microscopy. *Science* 2012, **336**, 444.

S8 M. Ternes, C. González, Ch. Lutz, P. Hapala, F. J. Giessibl, P. Jelínek and A. J. Heinrich, *Phys. Rev. Lett.* 2011, **106**, 016802.